THE JOURNAL OF PHYSICAL CHEMISTRY C
A JOURNAL OF THE AMERICAN CHEMICAL SOCIETY

pubs.acs.org/JPCC
Article

Electrochemical and Computational Insights into Lithium Nucleation on Single-Crystal Copper for Anode-Free Li-Metal Batteries

Katarina Cicvarić, Lars Mannich, Dmitrii Blum, Wang Hu, Susana Suttor, Vitaly Alexandrov, and Aliaksandr S. Bandarenka*

Cite This: https://doi.org/10.1021/acs.jpcc.5c07557
Read Online

ABSTRACT: Anode-free lithium (Li) metal batteries promise high energy density due to the absence of graphite on the anode side, whereby Li is directly electroplated onto the current collector during charging. Copper (Cu) foil is commonly used as a current collector; however, dendritic growth, which can cause catastrophic failure, is often observed. Optimizing nucleation is one of the proposed strategies for obtaining smooth, dendrite-free Li deposits. This work investigates nucleation of Li onto a Cu(111) single crystal by electrochemical impedance spectroscopy (EIS) and density functional theory (DFT) calculations. EIS allows for the monitoring of kinetic deposition parameters ($k_{app}(t,E)$) as a function of potential and time, offering a more profound insight into early stage deposition mechanisms. It is shown that $k_{app}(t,E)$ decreases with increasing deposition potential, while over the course of deposition a decrease can be observed during the initial stages of deposition. Furthermore, DFT calculations show a decreasing trend in adsorption strength with Li coverage, providing additional atomistic insights into the decreasing time-dependent behavior of the kinetic parameters.

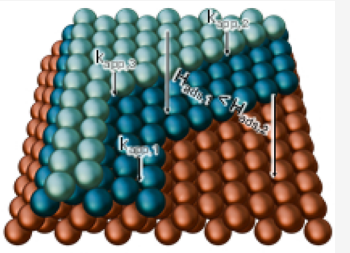

1. INTRODUCTION

Rechargeable batteries are essential for various technological applications, including consumer electronics, electric vehicles, and grid energy storage. Lithium-ion batteries, which currently dominate the market for rechargeable batteries, comprise an Al current collector/cathode material/separator/anode material/Cu current collector, with a liquid organic carbonate electrolyte infiltrating the porous electrodes and separator. Commercially available lithium-ion batteries have a gravimetric energy density of ∼280 Wh/kg and a volumetric energy density of ∼750 Wh/L, which cannot meet the ever-increasing demand for a higher energy density. One way to meet the demand is to remove the graphite at the anode side, in a cell configuration called the "anode-free Li-metal battery." As assembled, the anode-free Li-metal battery features only a Cu foil current collector at the anode side, where metallic Li is directly electroplated during charging and stripped and intercalated back into the cathode during discharging. The metallic Li anode is regarded as one of the most effective solutions, as it possesses several advantageous features, including a low atomic weight (6.94), the lowest reduction potential (−3.04 V vs SHE), and a low density (0.534 g/cm^3). The lack of graphite material allows for thinner cells with lower mass, increasing both the gravimetric and volumetric energy density to ∼420 Wh/kg and ∼1515 Wh/L, respectively.[1] Nevertheless, the practical realization of this cell configuration has still not been attained as it poses a substantial safety concern. Generally, while electroplating Li tends to form irregular structures, which have a high surface area and are prone to forming needlelike structures called "dendrites." Upon contact with conventional carbonate electrolytes, metallic Li undergoes passivation, forming a "solid−electrolyte interphase" (SEI) due to lithium's tendency to react with components of the electrolyte, leading to irreversible capacity loss. Furthermore, the formation of Li dendrites during electroplating can result in a cell short circuit, generating heat and potentially leading to a thermal runaway. Hence, it is of utmost importance to grow smooth and compact metallic Li on the Cu foil current collector while charging. Faster charging times are being intensively pursued; however, charging with a high constant current further exacerbates dendrite growth.[2−7]

Within anode-free Li-metal batteries, the anode current collector serves as a host for Li deposition during charging and simultaneously enables electron transfer between the external circuit and lithium. For this purpose, Cu, Ni, Ti, and stainless steel have been investigated as anode current collectors owing to their electrochemical stability in a potential range between 0 and 3 V vs Li/Li$^+$ and high electrical conductivity in the

Received: November 4, 2025
Revised: December 11, 2025
Accepted: December 23, 2025

following order: Cu (approximately 59 × 10^6 S m^{-1}) > Ni (14.4 × 10^6 S m^{-1}) > Ti (2.5 × 10^6 S m^1) > stainless steel (1.4 × 10^6 S m^{-1}).[8] Given its highest electrical conductivity and electrochemical stability, Cu is most frequently used as a current collector in Li-ion batteries. However, the lithiophobic nature of Cu leads to a substantial nucleation overpotential and rough Li deposits. Moreover, defect sites, such as grain boundaries, tips, and microcracks, induce nonuniform Li^+ flux, resulting in heterogeneous Li plating and dendrite growth.[9,10]

Nucleation is a first step in the Li deposition process, which largely determines the growth mode morphology of the deposited metallic Li, as undesirable nucleation kinetics resulting in uneven distribution of nuclei and out-of-plane growth orientation initiate dendritic growth. Consequently, altering the nucleation process presents a viable approach to address the origin of dendrite formation in the initial stages of Li deposition.[10−16] Pei et al. studied the early stages of nucleation, establishing an inversely proportional relationship between the nuclei radius and applied overpotential, meaning that the lower overpotential generates larger nuclei, favoring uniform deposition of metallic Li.[17] Heterogeneous nucleation of metallic Li on Cu was further investigated with various advanced characterization methods, such as electrochemical atomic force microscopy (EC-AFM),[18] Kelvin probe force microscopy (KPFM),[19] operando reflection interference microscope (RIM),[14] as a function of overpotential,[13,14,17] in different electrolytes correlating it to the chemical and physical properties of SEI,[20,21] by modification of Cu foil surface with lithophilic layers,[11,22−24] by 3D structuring Cu foil,[25−28] as a function of crystal orientation of Cu single crystals where it was shown that Li nuclei on Cu(111) have smallest and most uniform size.[29] When examining the metal nucleation electrochemically, one must also factor in the thermodynamic aspects of the system. In this regard, Pu et al. observed underpotential deposition of Li on Cu substrates commencing at high potentials but dropping significantly with coverage as a result of repulsion between Li adatoms.[30] Studies on the atomic level report surface mobility and rearrangement of Li adatoms on Cu surface, whereas Cu(111) orientation favors horizontal and homogeneous Li growth[31] as it possesses the lowest migration barrier compared to other low-index facets (e.g., Cu(100) and Cu(110)).[32,33] Røe et al. found almost 10 times higher surface diffusion barrier of Li adatom on Cu(001) than that on Li(001) due to the lattice mismatch between Li and Cu, rendering Li more prone to dendrite formation.[34] Rulev et al. hypothesize that surface diffusion in grain boundaries in polycrystalline Li could suppress dendritic growth.[35] Vishnugopi et al. identified interlayer diffusion as a governing mechanism in Mg electrodeposition, favoring the growth of smooth films, whereas Li, possessing a large barrier height for interlayer diffusion, forms dendrites.[36]

Herein, we explore the early stages of Li electrodeposition on a Cu(111) single crystal by electrochemical impedance spectroscopy (EIS), from which the so-called apparent rate coefficient of deposition $k_{app}(t,E)$ was calculated. Our results show that by increasing the deposition potential, $k_{app}(t,E)$ decreases, while within the same potential, a decrease in $k_{app}(t,E)$ can be observed during initial deposition, after which it stabilizes. In addition, we observe an underpotential deposition (UPD) of Li corresponding to the $\sim^1/_3$ of a Li monolayer prior to Li deposition. We further employ density functional theory (DFT) calculations to compute the adsorption energies during the initial UPD Li monolayer and subsequent second layer growth. Our findings show a decreasing trend of adsorption strength with increasing layer coverage degree, elucidating an experimentally observed decrease of $k_{app}(t,E)$ over time.

2. METHODS

2.1. General

All measurements were conducted in an Ar-filled glovebox (MBraun MB 200B, Germany). One M $LiPF_6$ (1 M) in ethylene carbonate:ethyl methyl carbonate 3:7, by wt. (E-Lyte, Germany) was used as an electrolyte. Commercial 15 mm diameter × 3 mm thickness Cu(111) single crystal (MaTeck GmbH, Germany) served as the working electrode, fixed in the electrochemical cell using a high-density polyethylene (HDPE) holder with a 10 mm diameter opening. As a counter electrode, a commercial 83 μm thick lithium ferrophosphate (aluminum foil single side coated by $LiFePO_4$, PI-KEM, UK) electrode was punched into 14 mm diameter circular pieces and fixed into the electrochemical cell using an HDPE holder with a 10 mm diameter opening. The potentials reported in this work were recorded with respect to Li used as the reference electrode. After the deposition experiments, Cu(111) single crystal was gently rinsed with ethyl methyl carbonate (E-Lyte, Germany) to remove residual salts. A PalmSens4 potentiostat (PalmSens, Netherlands) was used to run electrochemical measurements.

2.2. SEI Formation and EIS

Prior to EIS/deposition experiments, a stable solid-electrolyte interphase (SEI) was formed by cyclic voltammetry in the potential range between 3.55 and 0 V vs Li/Li^+ with a scan rate of 50 mV/s for 10 scans. EIS probed electrochemical interfaces with small 5−25 mV AC signals with 1 mV amplitude, within frequency ranges from 0.1 Hz to 100 kHz in time scan type for 3600 s for each overpotential, resulting in the acquisition of 26 impedance spectra. Analysis of the EIS spectra, including Kramers−Kronig check, circuit fitting, and parameter extraction, was carried out with EIS Spectrum Analyzer software.[37] Following the deposition, a cyclic voltammogram was recorded in a potential range between 3.55 and 0 V vs Li/Li^+ to identify the oxidation peak associated with Li stripping. By employing an oxidation potential, the deposited lithium was stripped.

2.3. Computational Details

The simulations of atomic-scale deposition of Li onto Cu were performed using the Vienna Ab initio Simulation Package (VASP) DFT code.[38,39] The Perdew-Burke-Ernzerhof (PBE) exchange-correlation functional[40] was used together with the projector augmented wave (PAW)[41,42] pseudopotentials for Li and Cu. A kinetic cutoff energy for the plane-wave basis set of 500 eV was employed together with a self-consistent field (SCF) convergence criterion of 10^{-6} eV. All geometries were relaxed to forces below 10^{-2} eV/Å. The Cu lattice constant was calculated to be 3.63 Å, which is in very good agreement with other DFT-calculated values.[43,44] The van der Waals dispersion energy-correction method DFT-D3[45] was used with the Becke−Johnson damping function[46] for all adsorption energy calculations. Supercells exposing the (111) facet along the z-direction were constructed with a size of p(2 × 2), p(3 × 3), and p(5 × 5) in the x−y plane, and the Brillouin zone was sampled using a Gamma-centered k-point grid of 13 × 13 × 1, 9 × 9 × 1, and 5 × 5 × 1, respectively. A vacuum separation along the z-direction of 15 Å was introduced to prevent

https://doi.org/10.1021/acs.jpcc.5c07557
J. Phys. Chem. C XXXX, XXX, XXX−XXX

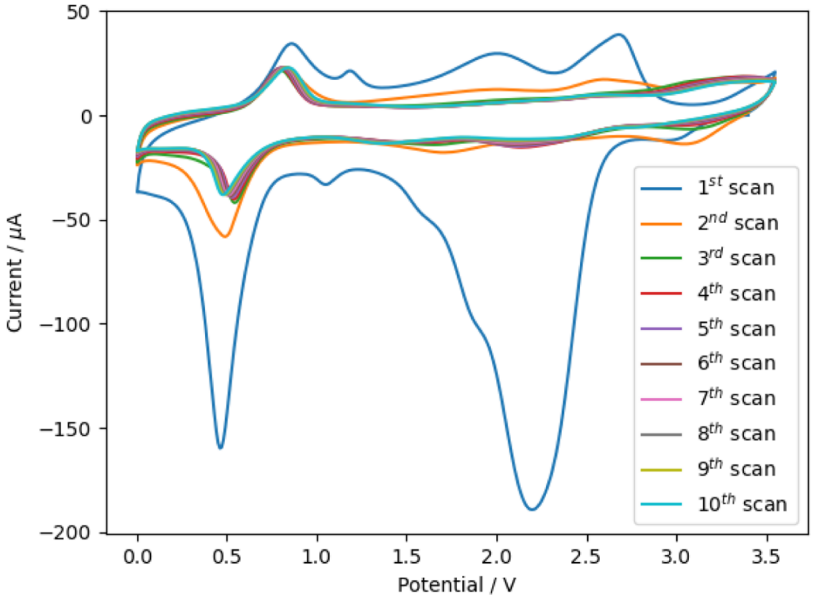

Figure 1. Ten cyclic voltammetry cycles of SEI formation on Cu(111) single crystal as the working electrode, LFP as the counter electrode, and Li as the reference electrode immersed in EC:EMC (3:7 by wt.) electrolyte. Scan rate is 0.05 V/s.

interactions between neighboring periodic images. The surface energy of Cu(111) was converged to a value of 1.31 J/m^2 with a Cu slab thickness of five layers (Figure S1), which is in good agreement with other DFT-calculated values.[47−50] The uppermost three layers of the Cu slab were allowed to relax for all of the calculations. Li was allowed to relax along the *z*-direction for the calculations of the adsorption energy of an individual Li atom and along all directions for the coverage calculations. The adsorption energies were calculated as follows:

$$E_{ads} = E_{n\text{Li@surf}} - E_{surf} - n \times E_{Li}$$

where $E_{n\text{Li@surf}}$, E_{surf}, E_{Li} and n are the total energies calculated by DFT extrapolated to 0 K for the surface with n adsorbed Li atoms, without the Li atoms, and the single Li atom, respectively. The adsorption energy of Li was converged at supercell sizes of p(5 × 5) and larger (Figure S2). The charge transfer between the Cu and Li layers was determined using Bader charge analysis.[51] The *VASP* precision setting was set to accurate to ensure a correct calculation of the atomic core charges.

3. RESULTS AND DISCUSSION

3.1. Electrodeposition of Li on Cu(111) Single Crystal

In an anode-free Li-metal battery, metallic Li is directly deposited onto the Cu current collector during charging. Prior to the deposition of metallic Li, a solid-electrolyte interphase (SEI) forms on the surface of the Cu current collector when the current is introduced. Herein, Cu(111) single crystal is chosen to exclude the effect of grain boundaries and crystalline defects, which can induce nucleation and promote dendrite growth.[32,] In addition, Li deposition is most favorable on (111) compared to other low-index facets (i.e., (100) and (110)).[29,30,52,53] The SEI was formed on Cu(111) single crystal by 10 cycles of cyclic voltammetry (CV) in the potential range between 0 and 3.55 V vs Li/Li$^+$, as shown in Figure 1. CVs were recorded in a three-electrode cell containing Cu(111) single crystal as working electrode, lithium ferrophosphate (LFP) as counter electrode, and metallic Li as reference electrode, immersed in 1 M $LiPF_6$ in ethylene carbonate:ethyl methyl carbonate (EC:EMC 3:7, by wt.) as electrolyte starting at open circuit potential (OCV), scanning toward 0 V, then back to 3.55 V vs Li/Li$^+$. The first scan features peaks corresponding to the SEI formation comprising the following compounds: the weak peak in the range of 2.5−3.1 V was identified as CuF_2 reduction resulting in LiF and Cu formation; the broad peaks between 2.5 and 1.5 V as Cu oxide reduction, Cu_xO lithiation, and LiF formation, and the peak around 0.5 V as the reduction of Li_2CO_3 to Li_2C_2 and Li_2O,[54] whereas in other sources, it was attributed to the underpotential deposition of Li on Cu.[55,56] In the reverse first scan, the small oxidation peaks represent Cu oxidation, which vanish after a stable SEI is formed on the Cu surface. We hypothesize that after the second scan, when no change is observed between the subsequent CVs and thus the SEI layer appears to be stable, the reduction peak at around 0.5 V represents underpotential deposition (UPD) of Li on Cu. In the reverse scan, we attribute the oxidation peak at approximately 0.9 V to the stripping of metallic Li. The charge passed for the UPD peak in the third scan for the area of 1 cm^2 is approximately 100 μC, corresponding to $\sim^1/_3$ of a Li monolayer. On the reverse scan, the charge calculated for the oxidation peak is approximately 80 μC, meaning that most of the underpotential deposited Li is stripped. Indeed, UPD is commonly observed in heterogeneous depositions, as the bonds between the adsorbate and substrate are stronger than those in bulk metal interactions.[30]

By applying an overpotential to the electrode at which metal deposition takes place, the electrode/electrolyte interface changes. Various deposition sites, such as terraces, steps, kinks, vacancies, etc., contribute to interface changes with their characteristic local rate coefficient of deposition and local current density $k_{app,1}(t,E)$, ..., $k_{app,i}(t,E)$. The overall $k_{app}(t,E)$ can therefore be approximated by the following Equation:

$$k_{app}(t, E) = \frac{n_1 k_{app,1}(t, E) + \ldots + n_i k_{app,i}(t, E)}{n(\text{total})}$$

https://doi.org/10.1021/acs.jpcc.5c07557
J. Phys. Chem. C XXXX, XXX, XXX−XXX

where n(total) is the overall number of active sites at the surface.

In the early stage of metal deposition on a substrate surface, adatoms can be deposited at energetically more favorable sites. Different types of active sites are shown in Figure 2: terrace ($k_{app,1}$), step edge ($k_{app,2}$), kink ($k_{app,3}$ and $k_{app,4}$), and vacancies ($k_{app,5}$ and $k_{app,6}$). Generally, it is assumed that the most favorable deposition sites are located at the kink sites; therefore, an adatom can directly incorporate into the kink sites, diffuse along the step edge toward kink sites, or diffuse from the terrace via the step edge until it finds a kink site.[57] After nucleation at different active nucleation sites, growth of metallic film dominates decreasing the contribution of local apparent rate coefficient ($k_{app,i}$) to the overall apparent coefficient (k_{app}), as shown in Figure 2. $k_{app}(t,E)$ can thus be defined as the rate at which electrochemical reactions take place at the electrode with respect to an "averaged" local deposition site.[44]

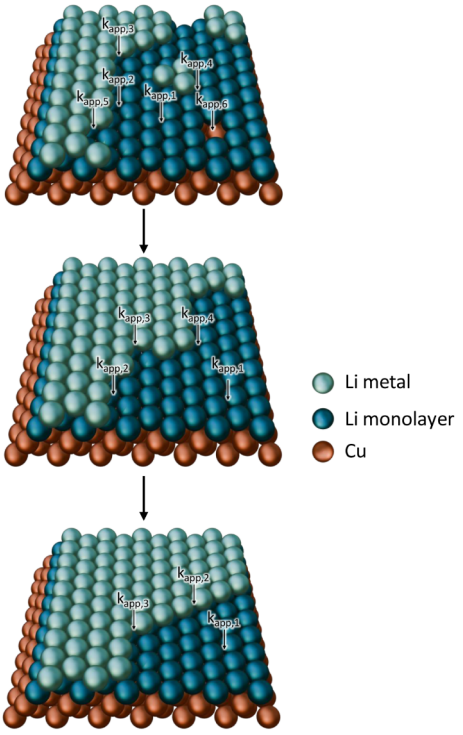

Figure 2. Schematic illustration of local apparent rate coefficients ($k_{app,i}$) and their contribution to the overall apparent rate coefficients (k_{app}) during metallic Li film growth at the Cu(111) surface. The local apparent rate coefficients ($k_{app,i}$) represent different active sites for Li nucleation: terrace ($k_{app,1}$), step edge ($k_{app,2}$), kink ($k_{app,3}$ and $k_{app,4}$), and vacancies ($k_{app,5}$ and $k_{app,6}$). The scheme illustrates how the initial active site *types* decrease as the film grows (the *total number* of deposition sites can, at the same time, increase).

To extract kinetic parameters, namely apparent rate coefficients $k_{app}(t,E)$ of Li deposition on Cu, potentiostatic electrodeposition was carried out at the following overpotentials: −5, −10, −15, −20, and −25 mV. The apparent rate coefficient of deposition ($k_{app}(t,E)$) can be calculated from the Equation:

$$k_{app}(t, E) = \sqrt{2D}\,\frac{A_W(t, E)}{R_{CT}(t, E)}$$

where $A_w(t,E)$ represents the Warburg coefficient and $R_{CT}(t,E)$ charge transfer resistance obtained from the impedance experiments, and D is the diffusion coefficient of the electroactive species. The $A_w(t,E)$ and $R_{CT}(t,E)$ can be expressed by the following Equations:

$$A_W = \frac{RT}{n^2F^2}\,\frac{1}{\alpha\sqrt{2D}\,C_S(t, E)A_{SC}(t, E)}$$

$$R_{CT} = \frac{RT}{n^2F^2}\,\frac{1}{\alpha k_{app}(t, E)C_S(t, E)A_{SC}(t, E)}$$

where $C_s(t,E)$ represents the surface concentration of electrochemically active species in the electrolyte and $A_{SC}(t,E)$—"active" geometric surface area of the electrode, both changing with time and electrode potential. A key outcome of computing $k_{app}(t,E)$ is the elimination of surface concentration and area, thereby demonstrating the relative influence of local rate coefficients at various active sites.[58] The A_W and R_{CT} are extracted by fitting the impedance spectra to a suggested equivalent electrical circuit (EEC) of the physical model, as shown in Figure 3.

In the EEC, R_u represents the uncompensated resistance stemming from contact, cabling, and electrolyte resistance. The SEI layer formed on the Cu surface is represented by the SEI capacitance (C_{SEI}) and resistance (R_{SEI}). Due to the electronically insulating but ionically conducting nature of SEI, Li ions diffuse through the layer and deposit on the Cu surface, the process comprising double-layer capacitance (C_{DL}), charge transfer resistance (R_{CT}), and Warburg element (W) in the physics-based EEC model. The diffusion-limited transport of Li ions represented by W stems from diffusion in the electrolyte and SEI layer, which cannot be distinguished by the physical model.[59,60]

Electrochemical impedance data collected during the deposition at different potentials and their corresponding fittings to the suggested EEC model are presented in Figure 4. The model provides a good fit for all measured overpotentials with RMS deviations typically in the range of a few percent, similar to.[44−46].

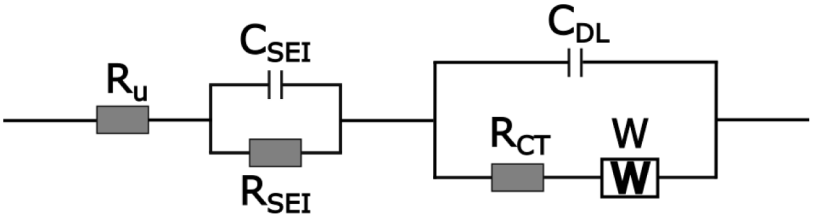

Figure 3. Suggested equivalent electric circuit (EEC) modeling the interface during electrodeposition of Li on Cu(111) single crystal working electrode from EC:EMC (3:7 by wt) electrolyte with LFP as counter electrode and metallic Li as reference electrode.

https://doi.org/10.1021/acs.jpcc.5c07557
J. Phys. Chem. C XXXX, XXX, XXX−XXX

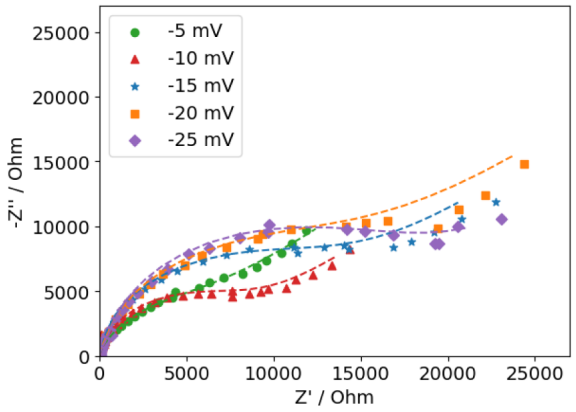

Figure 4. Typical electrochemical impedance spectra of deposition of Li at different potentials recorded on Cu(111) single crystal working electrode in EC:EMC (3:7 by wt) electrolyte with LFP as counter electrode and metallic Li as reference electrode. Dashed lines are fittings of the respective data. The experimental data are displayed as symbols in Nyquist plots (imaginary impedance, $-Z''$, versus real impedance, Z'), and fitted curves (dashed lines) were obtained using the proposed EEC.

The calculated k_{app} values at five different potentials with time are shown in Figure 5a. For each potential, 26 impedance spectra were recorded over the course of deposition, from which k_{app} values were calculated. At the lowest potential of −5 mV, k_{app} initially increases up to about 300 s, whereas at higher overpotentials, an opposite behavior is observed, where k_{app} initially decreases. Afterward, k_{app} decreases slightly for −5 mV, while for other potentials, it remains almost constant. This change in k_{app} during the early stage of deposition reveals varying contributions from local deposition rates. In the later stages of deposition, the contribution from different deposition sites stabilizes or changes only slightly in the case of −5 mV, while the overall number of active sites increases over time. Therefore, these findings highlight the significance of the early stages of deposition and the potential for adjusting the properties of the deposits by optimizing the early stage of film growth. Figure 5b shows the change in average k_{app} value calculated after stabilization (here taken after 2000 s) with standard deviation as error bars. It can be seen that the highest drop in k_{app} is between −5 and −10 mV, while between −10 and −25 mV the drop only slightly. These results indicate that lower overpotentials and shorter deposition times have significantly higher contributions to the total k_{app} as more of the various deposition sites are active. We hypothesize that this behavior is also due to lower diffusion limitations at lower overpotentials and shorter deposition times. Namely, at higher overpotentials and longer deposition times, an ion depletion region forms in close proximity to the electrode due to the ion diffusion limitation, enabling higher ion mobility along the surface. Consequently, ions diffuse along the surface to energetically more favorable active sites, which ultimately decreases the overall k_{app}.[61]

3.2. Calculations

To gain further insights into the initial stages of Li deposition and nucleation on the Cu(111) single-crystal surface, density functional theory (DFT) calculations were employed. The modeled electrochemical adsorption reaction is

$$Li^+ + e^- + * \rightarrow Li^*$$

where * denotes an adsorption site on the metal surface. The four symmetrically distinct adsorption sites on the Cu(111) facet (top, bridge, hollow (hcp), and hollow (fcc)—were tested for the initial adsorption of a single Li atom. The calculated adsorption energies for each site are presented in Table 1. The hollow sites (hcp and fcc) were found to be energetically equivalent and the most favorable for Li adsorption.

Table 1. Adsorption Energies of a Single Li Atom at Different Adsorption Sites on the Bare Cu(111) Surface

	Adsorption Site			
	Top	Bridge	Hollow (hcp)	Hollow (fcc)
Adsorption Energy/eV	−2.51	−2.62	−2.63	−2.63

Li atoms were subsequently adsorbed onto the Cu (111) surface at different surface coverages θ with all atoms placed at the hollow (fcc) adsorption sites. Figure 6a and b illustrate the configurations employed to model different coverages using the p(2 × 2) and p(3 × 3) supercells, respectively. The corresponding average adsorption energies per Li atom are presented in Figure 6c. For reference, the adsorption energy of

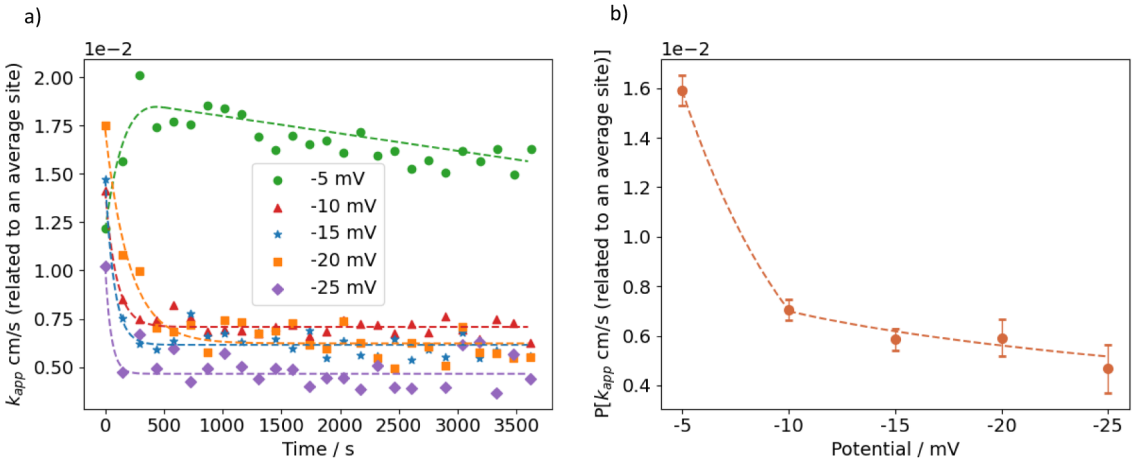

Figure 5. a) Dependence of k_{app} on deposition time and potential. b) Dependence of average k_{app} with deposition potential after stabilization (2000 s) with standard deviation as error bars. Dashed lines are guides for the eyes.

https://doi.org/10.1021/acs.jpcc.5c07557
J. Phys. Chem. C XXXX, XXX, XXX−XXX

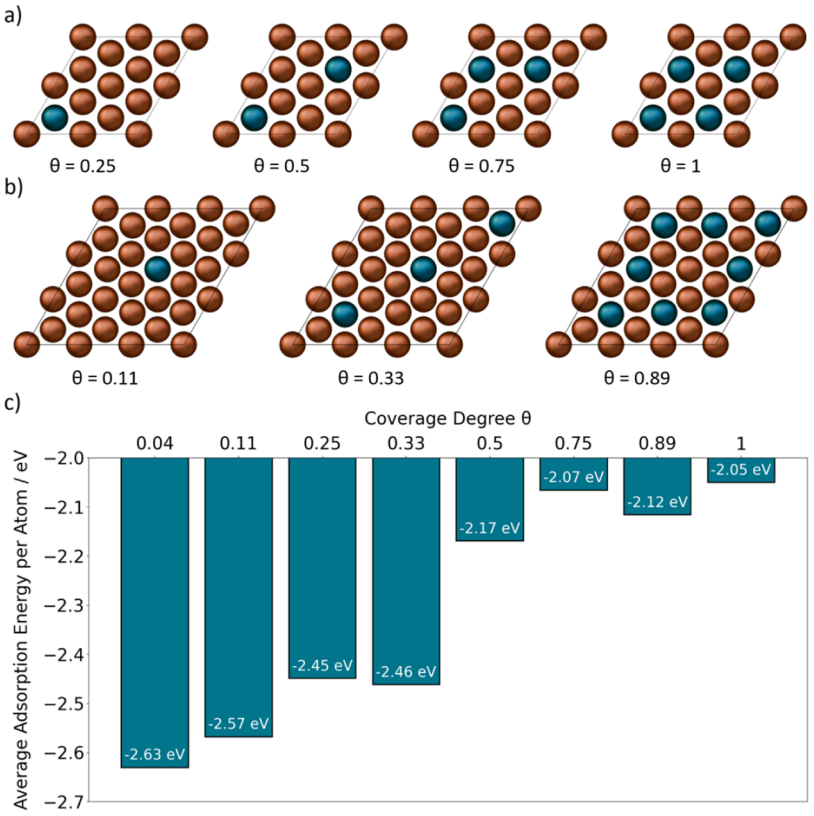

Figure 6. Simulation of different coverages of Li on the Cu(111) surface. a) Top view on the p(2 × 2) systems used to evaluate the θ = 1, 0.75, 0.5, and 0.25 surface coverages. b) Top view on the p(3 × 3) systems used to evaluate the θ = 0.89, 0.33, and 0.11 coverages. c) Average adsorption energy of Li for different monolayer surface coverages.

an isolated Li atom in a p(5 × 5) cell (θ = 0.04) is also included. A general increase (from more negative to less negative) in adsorption energy is observed with increasing coverage, from −2.63 eV at θ = 0.04 to −2.05 eV at θ = 1. Notably, a significant rise in adsorption energy occurs between θ = 0.33 and 0.5, indicating a transition toward a highly close-packed arrangement, which is energetically less favorable for Li deposition.

While experimental SEI formation showed UPD of Li, indicating the formation of an ∼1/3 monolayer, we further assume a coverage of θ = 1, as the other cases (the completion of the monolayer at the initial stages of Li deposition) are analyzed above. This represents an idealized adlayer, whereas the growth of a second Li layer was modeled analogously. The adsorption site preference for a single Li atom deposited onto the complete UPD layer (θ = 1) was first evaluated, with the corresponding adsorption energies summarized in Table 2. Although the top site was identified as the most energetically favorable, the small energy differences relative to other sites suggest that the site preference is not thermodynamically significant.

Table 2. Adsorptionenergy of a Single Li Atom at Different Adsorption Sites on the Cu(111) Surface with a Li Adlayer Coverage of θ = 1

	Adsorption Site			
	Top	Bridge	Hollow (hcp)	Hollow (fcc)
Adsorption Energy/eV	−2.06	−2.04	−2.03	−2.04

Extending the previous methodology, a second Li layer with different coverages was subsequently adsorbed onto the monolayer-covered Cu (111) surface with each Li atom placed at a top site. The same range of surface coverages was considered as that for the first layer. The corresponding average adsorption energies per Li atom in the second layer are shown in Figure 7. A continuous trend up in adsorption energy is again observed with increasing coverage degrees, ranging from −2.06 eV at θ = 0.04 to −1.69 eV at θ = 1. Similar to the first layer, a pronounced change in adsorption energy occurs between θ = 0.33 and θ = 0.5. However, in contrast to the initial layer, the adsorption energy stabilizes at coverages of θ = 0.33 and below, forming a plateau at approximately −1.99 eV up until a coverage of θ = 0.11. This behavior of adsorption energies with increasing coverage degrees could be the basis of the experimentally observed decrease in $k_{app}(t,E)$ over time in early stages of deposition.

To gain further insights into the interfacial behavior of Cu and Li, the distribution of electronic charges was evaluated using Bader charge analysis. As illustrated in Figure 8a, each Li atom of the first deposited layer (θ = 1) was found to have a remaining partial charge of +0.7 e, while the Cu atoms located in the uppermost layer obtained the opposite partial charge of −0.7 e. This suggests an electrostatic repulsion between atoms in the same layer, where the remaining partial charges of the same sign increase in strength as the atoms are located closer to each other. In combination with the lattice mismatch between Cu and Li, this could increase the adsorption energy for denser configurations. A different charge transfer character compared to that of the first layer was found after adsorption of the second Li layer, as shown in Figure 8b. While the UPD

https://doi.org/10.1021/acs.jpcc.5c07557
J. Phys. Chem. C XXXX, XXX, XXX−XXX

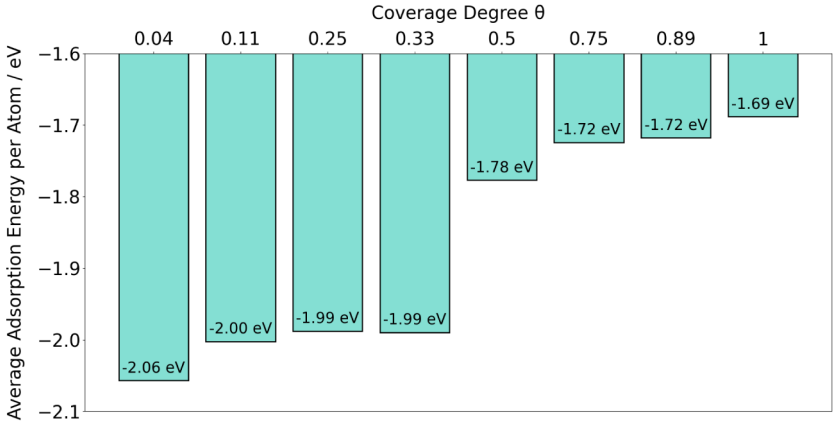

Figure 7. Average adsorption energy per Li atom for different coverages of subsequent second-layer Li deposition on Cu(111) covered with an initial UPD Li layer at a coverage of $\theta = 1$.

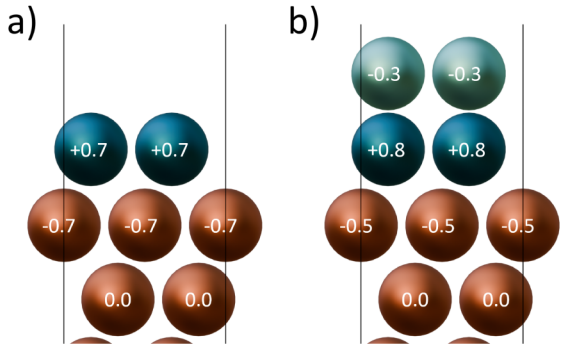

Figure 8. Distribution of electronic charges in the deposited Li and uppermost Cu layers. a) Bader charge of Cu and Li for monolayer UPD with a coverage of $\theta = 1$. b) Bader charge of Cu and Li for second-layer coverage of $\theta = 1$.

Li atoms obtain a relatively similar partial charge of +0.8 e (compared to +0.7 e previously), the opposite partial charges were found to be located both at the Cu atoms in the uppermost layer (−0.5 e per atom) as well as within the second Li layer (−0.3 e per atom). The decrease in absolute net partial charge of the Li atoms moving from the first layer to the second layer could explain the smaller overall increase in adsorption energy for the different coverage degrees of the second layer (by ca. 0.37 eV) compared to the first layer (by ca. 0.58 eV).

4. CONCLUSIONS

A physical mechanism of early stage deposition of Li onto the Cu(111) single crystal was proposed based on $k_{app}(t,E)$ measurements and DFT calculations. EIS at varying deposition potentials was employed to calculate $k_{app}(t,E)$, revealing a decrease in $k_{app}(t,E)$ with applied overpotential. Furthermore, at the same potential, a decrease in $k_{app}(t,E)$ over time can be observed during the initial deposition, after which it mainly remains constant. This insight emphasizes the importance of early stage deposition on the quality of deposits, which is crucial for the performance of anode-free Li-metal batteries. In addition, we observed an UPD of Li on Cu(111) corresponding to $\sim^1/_3$ of the monolayer prior to Li deposition. DFT calculations further revealed a decrease in adsorption strength with increasing surface coverage for both the first and second Li layer deposition. This behavior could explain the decrease in $k_{app}(t,E)$ over time, which was observed experimentally during the initial stages of deposition. Furthermore, the calculations revealed that the partial charge of Li atoms in the first layer is higher than in the subsequent layer, resulting in a stronger repulsion between neighboring atoms and an energetically less favorable state. Therefore, the difference in adsorption strength between an individual adsorbed Li atom and a close-packed Li-covered surface is larger for the first layer. The repulsion might account for the significant rise in adsorption energy observed moving from $\theta = 0.33$ to $\theta = 0.5$ coverage in the first layer, offering a better understanding of the incomplete monolayer formed during UPD. We further assume that the difference in adsorption energies could result from both lattice mismatch and differences in partial charge.

■ ASSOCIATED CONTENT

Supporting Information

The Supporting Information is available free of charge at https://pubs.acs.org/doi/10.1021/acs.jpcc.5c07557.

Convergence of the Cu(111) slab surface energy with respect to the number of Cu layers. Convergence of the adsorption energy with respect to the supercell size (PDF)

■ AUTHOR INFORMATION

Corresponding Author

Aliaksandr S. Bandarenka − *Physics of Energy Conversion and Storage, Department of Physics, Technical University of Munich, Garching 85748, Germany;* orcid.org/0000-0002-5970-4315; Email: bandarenka@ph.tum.de

Authors

Katarina Cicvarić − *Physics of Energy Conversion and Storage, Department of Physics, Technical University of Munich, Garching 85748, Germany*

Lars Mannich − *Physics of Energy Conversion and Storage, Department of Physics, Technical University of Munich, Garching 85748, Germany*

Dmitrii Blum − *Physics of Energy Conversion and Storage, Department of Physics, Technical University of Munich, Garching 85748, Germany*

https://doi.org/10.1021/acs.jpcc.5c07557
J. Phys. Chem. C XXXX, XXX, XXX−XXX

Wang Hu − *Physics of Energy Conversion and Storage, Department of Physics, Technical University of Munich, Garching 85748, Germany*

Susana Suttor − *Physics of Energy Conversion and Storage, Department of Physics, Technical University of Munich, Garching 85748, Germany; BMW AG, Munich 80809, Germany;* orcid.org/0000-0001-6096-2090

Vitaly Alexandrov − *Department of Chemical and Biomolecular Engineering, University of Nebraska-Lincoln, Lincoln, Nebraska 68588, United States;* orcid.org/0000-0003-2063-6914

Complete contact information is available at: https://pubs.acs.org/10.1021/acs.jpcc.5c07557

Notes

The authors declare no competing financial interest.

■ ACKNOWLEDGMENTS

The project received funding from the DFG (Excellence Cluster "e-conversion", Excellence Strategy − EXC 2089/1 − 390776260). The authors also acknowledge the support of the Technical University of Munich (TUM) Laura Bassi scholarship and the German Academic Exchange Service (DAAD) scholarship.

■ REFERENCES

(1) Heubner, C.; Maletti, S.; Auer, H.; Hüttl, J.; Voigt, K.; Lohrberg, O.; Nikolowski, K.; Partsch, M.; Michaelis, A. From Lithium-Metal toward Anode-Free Solid-State Batteries: Current Developments, Issues, and Challenges. *Adv. Funct. Mater.* **2021**, *31* (51), 2106608.

(2) Salvatierra, R. V.; Chen, W.; Tour, J. M. What Can be Expected from "Anode-Free" Lithium Metal Batteries? *Adv. Energy Sustainability Res.* **2021**, *2* (5), 2000110.

(3) Nanda, S.; Gupta, A.; Manthiram, A. Anode-Free Full Cells: A Pathway to High-Energy Density Lithium-Metal Batteries. *Adv. Energy Mater.* **2021**, *11* (2), 2000804.

(4) Lin, L.; Qin, K.; Hu, Y. S.; Li, H.; Huang, X.; Suo, L.; Chen, L. A Better Choice to Achieve High Volumetric Energy Density: Anode-Free Lithium-Metal Batteries. *Adv. Mater.* **2022**, *34* (23), 2110323.

(5) Tang, K.; Tian, L.; Zhang, Y.; Xu, Z. J. Anode-free lithium metal batteries: a promising flexible energy storage system. *J. Mater. Chem. A* **2024**, *12* (27), 16268−16292.

(6) Jo, C.-H.; Sohn, K.-S.; Myung, S.-T. Feasible approaches for anode-free lithium-metal batteries as next generation energy storage systems. *Energy Storage Mater.* **2023**, *57*, 471−496.

(7) Xiong, S.; Nyholm, L.; Matic, A.; Zhang, C. Lithium electrodeposition for energy storage: filling the gap between theory and experiment. *Mater. Today Energy* **2022**, *28*, 101060.

(8) Rezaee, S.; Araghi, H.; Noshad, H.; Zabihi, Z. Physical characteristics of nickel thin-films and nickel thin-film foams as Li-air batteries anode and cathode current collectors. *J. Mol. Liq.* **2023**, *383*, 122171.

(9) Qiu, J.; Qiu, R.; Mao, Z.; Han, Y.; Madhusudan, P.; Wang, X.; Wang, C.; Qi, C.; Yu, X.; Zeng, S.; et al. A review on copper current collector used for lithium metal batteries: Challenges and strategies. *J. Energy Storage* **2024**, *100*, 113683.

(10) Guan, X.; Wang, A.; Liu, S.; Li, G.; Liang, F.; Yang, Y.-W.; Liu, X.; Luo, J. Controlling Nucleation in Lithium Metal Anodes. *Small* **2018**, *14* (37), 1801423.

(11) Du, R.; Jie, Y.; Chen, Y.; Huang, F.; Cai, W.; Liu, Y.; Li, X.; Wang, S.; Lei, Z.; Cao, R.; Zhang, G.; Jiao, S. Modulating Lithium Nucleation Behavior through Ultrathin Interfacial Layer for Superior Lithium Metal Batteries. *ACS Appl. Energy Mater.* **2020**, *3* (7), 6692−6699.

(12) Lin, L.; Zheng, H.; Luo, Q.; Lin, J.; Wang, L.; Xie, Q.; Peng, D.-L.; Lu, J. Regulating Lithium Nucleation at the Electrolyte/Electrode Interface in Lithium Metal Batteries. *Adv. Funct. Mater.* **2024**, *34* (24), 2315201.

(13) Ely, D. R.; García, R. E. Heterogeneous Nucleation and Growth of Lithium Electrodeposits on Negative Electrodes. *J. Electrochem. Soc.* **2013**, *160* (4), A662−A668.

(14) Wang, S.; Yin, X.; Liu, D.; Liu, Y.; Qin, X.; Wang, W.; Zhao, R.; Zeng, X.; Li, B. Nanoscale observation of the solid electrolyte interface and lithium dendrite nucleation-growth process during the initial lithium electrodeposition. *J. Mater. Chem. A* **2020**, *8* (35), 18348−18357.

(15) Ye, L.; Zhang, C.; Zhou, Y.; Ülgüt, B.; Zhao, Y.; Qian, J. Guided lithium nucleation and growth on lithiophilic tin-decorated copper substrate. *J. Energy Chem.* **2022**, *74*, 412−419.

(16) Wang, Y.; Tan, J.; Li, Z.; Ma, L.; Liu, Z.; Ye, M.; Shen, J. Recent progress on enhancing the Lithiophilicity of hosts for dendrite-free lithium metal batteries. *Energy Storage Mater.* **2022**, *53*, 156−182.

(17) Pei, A.; Zheng, G.; Shi, F.; Li, Y.; Cui, Y. Nanoscale Nucleation and Growth of Electrodeposited Lithium Metal. *Nano Lett.* **2017**, *17* (2), 1132−1139.

(18) To-A-Ran, W.; Mastoi, N. R.; Ha, C. Y.; Song, Y. J.; Kim, Y. J. Kelvin Probe Force Microscopy and Electrochemical Atomic Force Microscopy Investigations of Lithium Nucleation and Growth: Influence of the Electrode Surface Potential. *J. Phys. Chem. Lett.* **2024**, *15* (28), 7265−7271.

(19) Feng, G.; Shi, Y.; Jia, H.; Risal, S.; Yang, X.; Ruchhoeft, P.; Shih, W.-C.; Fan, Z.; Xu, W.; Shan, X. Progressive and instantaneous nature of lithium nucleation discovered by dynamic and operando imaging. *Sci. Adv.* **2023**, *9* (21), No. eadg6813.

(20) Park, H.; Jeon, Y.; Chung, W. J.; Bae, Y.; Kim, J.; Baek, H.; Park, J. Early Stage Li Plating by Liquid Phase and Cryogenic Transmission Electron Microscopy. *ACS Energy Lett.* **2023**, *8* (1), 715−721.

(21) Wang, M.; Ren, Z.; Lin, H.; Peng, Z.; Li, Z.; Li, H.; Shen, Y.; He, H.; Wang, D.; Zheng, J.; Wang, M. Realizing Compact Lithium Deposition via Elaborative Nucleation and Growth Regulation for Stable Lithium-Metal Batteries. *ACS Appl. Mater. Interfaces* **2021**, *13* (29), 34248−34257.

(22) Li, N.; Ye, Q.; Zhang, K.; Yan, H.; Shen, C.; Wei, B.; Xie, K. Normalized Lithium Growth from the Nucleation Stage for Dendrite-Free Lithium Metal Anodes. *Angew. Chem., Int. Ed.* **2019**, *58* (50), 18414−18419.

(23) Hou, Z.; Yu, Y.; Wang, W.; Zhao, X.; Di, Q.; Chen, Q.; Chen, W.; Liu, Y.; Quan, Z. Lithiophilic Ag Nanoparticle Layer on Cu Current Collector toward Stable Li Metal Anode. *ACS Appl. Mater. Interfaces* **2019**, *11* (8), 8148−8154.

(24) Huang, S.; Meng, C.; Chen, H.; Jiao, Z.; Qiu, J.; Zhu, H.; Shi, F.; Yuan, A.; Zhou, H. Self-assembled monolayer regulates lithium nucleation and growth for stable lithium metal anodes. *Electrochim. Acta* **2024**, *482*, 143998.

(25) Tang, Y.; Shen, K.; Lv, Z.; Xu, X.; Hou, G.; Cao, H.; Wu, L.; Zheng, G.; Deng, Y. Three-dimensional ordered macroporous Cu current collector for lithium metal anode: Uniform nucleation by seed crystal. *J. Power Sources* **2018**, *403*, 82−89.

(26) Gao, T.; Xu, D.; Yu, Z.; Huang, Z. H.; Cheng, J.; Yang, Y. A 3D lithium metal anode reinforced by scalable in-situ copper oxide nanostick copper mesh. *J. Alloys Compd.* **2021**, *865*, 158908.

(27) Zhao, Y.; Hao, S.; Su, L.; Ma, Z.; Shao, G. Hierarchical Cu fibers induced Li uniform nucleation for dendrite-free lithium metal anode. *Chem. Eng. J.* **2020**, *392*, 123691.

(28) Liu, C.; Wu, B.; Zhang, Y.; Liu, T.; Cui, J.; Huang, L.; Tan, G.; Zhang, L.; Su, Y.; Wu, F. Dense cuprous oxide sheath decorated three-dimensional copper foam enabling stable lithium metal anodes. *J. Mater. Chem. A* **2023**, *11* (46), 25455−25464.

(29) Ishikawa, K.; Ito, Y.; Harada, S.; Tagawa, M.; Ujihara, T. Crystal Orientation Dependence of Precipitate Structure of Electrodeposited Li Metal on Cu Current Collectors. *Cryst. Growth Des.* **2017**, *17* (5), 2379−2385.

(30) Pu, J. K.; Viswanathan, V. Thermodynamic Origin of Li Underpotential and Overpotential Deposition on Current Collectors. *J. Phys. Chem. C* **2025**, *129*, 7677.
(31) Lai, G.; Jiao, J.; Fang, C.; Jiang, Y.; Sheng, L.; Xu, B.; Ouyang, C.; Zheng, J. The Mechanism of Li Deposition on the Cu Substrates in the Anode-Free Li Metal Batteries. *Small* **2023**, *19* (3), 2205416.
(32) Kim, M. H.; Kim, D. Y.; Li, Y.; Kim, J.; Kim, M. H.; Seo, J.; Cunning, B. V.; Kim, T.; Park, S. W.; Ruoff, R. S.; Seo, D. H.; Jin, S.; Lee, H. W. Horizontal lithium growth driven by surface dynamics on single crystal Cu(111) foil. *Energy Environ. Sci.* **2024**, *17*, 6521.
(33) Li, G.; Shi, D.; Hao, Z.; Lu, Y.; Zhao, Q.; Yan, Z.; Xie, W.; Meng, X.; Chen, J. Computational Insights into the Crystal Facet Selectivity of Cu Current Collector for the Growth of Lithium Metal. *J. Phys. Chem. C* **2023**, *127* (33), 16297−16303.
(34) Røe, I. T.; Schnell, S. K. Slow surface diffusion on Cu substrates in Li metal batteries. *J. Mater. Chem. A* **2021**, *9* (17), 11042−11048.
(35) Rulev, A. A.; Kondratyeva, Y. O.; Yashina, L. V.; Itkis, D. M. Lithium Planar Deposition vs Whisker Growth: Crucial Role of Surface Diffusion. *J. Phys. Chem. Lett.* **2020**, *11* (24), 10511−10518.
(36) Vishnugopi, B. S.; Hao, F.; Verma, A.; Mukherjee, P. P. Surface diffusion manifestation in electrodeposition of metal anodes. *Phys. Chem. Chem. Phys.* **2020**, *22* (20), 11286−11295.
(37) Bandarenka, A. S. Development of hybrid algorithms for EIS data fitting. In *Lecture Notes on Impedance Spectroscopy. Measurement, Modelling and Applications*, Kanoun, O., ed.; CRC Press: London, 2013; Vol. *4*, pp. 29−36.
(38) Kresse, G.; Furthmüller, J. Efficiency of ab-initio total energy calculations for metals and semiconductors using a plane-wave basis set. *Comput. Mater. Sci.* **1996**, *6* (1), 15−50.
(39) Kresse, G.; Furthmüller, J. Efficient iterative schemes for ab initio total-energy calculations using a plane-wave basis set. *Phys. Rev. B* **1996**, *54* (16), 11169−11186.
(40) Perdew, J. P.; Burke, K.; Ernzerhof, M. Generalized Gradient Approximation Made Simple. *Phys. Rev. Lett.* **1996**, *77* (18), 3865−3868.
(41) Blöchl, P. E. Projector augmented-wave method. *Phys. Rev. B* **1994**, *50* (24), 17953−17979.
(42) Kresse, G.; Joubert, D. From ultrasoft pseudopotentials to the projector augmented-wave method. *Phys. Rev. B* **1999**, *59* (3), 1758−1775.
(43) Haas, P.; Tran, F.; Blaha, P. Calculation of the lattice constant of solids with semilocal functionals. *Phys. Rev. B* **2009**, *79* (8), 085104.
(44) Jain, A.; Ong, S. P.; Hautier, G.; Chen, W.; Richards, W. D.; Dacek, S.; Cholia, S.; Gunter, D.; Skinner, D.; Ceder, G.; et al. Commentary: The Materials Project: A materials genome approach to accelerating materials innovation. *APL Mater.* **2013**, *1* (1), 011002.
(45) Grimme, S.; Antony, J.; Ehrlich, S.; Krieg, H. A consistent and accurate *ab initio* parametrization of density functional dispersion correction (DFT-D) for the 94 elements H-Pu. *J. Chem. Phys.* **2010**, *132* (15), 154104.
(46) Grimme, S.; Ehrlich, S.; Goerigk, L. Effect of the damping function in dispersion corrected density functional theory. *J. Comput. Chem.* **2011**, *32* (7), 1456−1465.
(47) Tran, R.; Xu, Z.; Radhakrishnan, B.; Winston, D.; Sun, W.; Persson, K. A.; Ong, S. P. Surface energies of elemental crystals. *Sci. Data* **2016**, *3*, 160080.
(48) Pande, V.; Viswanathan, V. Computational screening of current collectors for enabling anode-free lithium metal batteries. *ACS Energy Lett.* **2019**, *4* (12), 2952−2959.
(49) Montoya, J. H.; Persson, K. A. A high-throughput framework for determining adsorption energies on solid-surfaces. *npj Comput. Mater.* **2017**, *3* (1), 14.
(50) Singh-Miller, N. E.; Marzari, N. Surface energies, work functions, and surface relaxations of low-index metallic surfaces from first principles. *Phys. Rev. B* **2009**, *80* (23), 235407.
(51) Tang, W.; Sanville, E.; Henkelman, G. A grid-based Bader analysis algorithm without lattice bias. *J. Phys.: Condens. Matter* **2009**, *21* (8), 084204.
(52) Qian, L.; Zheng, Y.; Or, T.; Park, H. W.; Gao, R.; Park, M.; Ma, Q.; Luo, D.; Yu, A.; Chen, Z. Advanced Material Engineering to Tailor Nucleation and Growth towards Uniform Deposition for Anode-Less Lithium Metal Batteries. *Small* **2022**, *18* (50), 2205233.
(53) Kim, Y.-J.; Kwon, S. H.; Noh, H.; Yuk, S.; Lee, H.; Jin, H. S.; Lee, J.; Zhang, J.-G.; Lee, S. G.; Guim, H.; et al. Facet selectivity of Cu current collector for Li electrodeposition. *Energy Storage Mater.* **2019**, *19*, 154−162.
(54) Menkin, S.; Okeefe, C. A.; Gunnarsdóttir, A. B.; Dey, S.; Pesci, F. M.; Shen, Z.; Aguadero, A.; Grey, C. P. Toward an Understanding of SEI Formation and Lithium Plating on Copper in Anode-Free Batteries. *J. Phys. Chem. C* **2021**, *125* (30), 16719−16732.
(55) Myung, S. T.; Sasaki, Y.; Sakurada, S.; Sun, Y. K.; Yashiro, H. Electrochemical behavior of current collectors for lithium batteries in non-aqueous alkyl carbonate solution and surface analysis by ToF-SIMS. *Electrochim. Acta* **2009**, *55* (1), 288−297.
(56) Myung, S. T.; Hitoshi, Y.; Sun, Y. K. Electrochemical behavior and passivation of current collectors in lithium-ion batteries. *J. Mater. Chem.* **2011**, *21* (27), 9891−9911.
(57) Paunovic, M.; Schlesinger, M. *Fundamentals of Electrochemical Deposition*, 2nd ed; John Wiley & Sons, Inc: Pennington, NJ, 2005. DOI: .
(58) Berkes, B. B.; Henry, J. B.; Huang, M.; Bondarenko, A. S. Electrochemical characterisation of copper thin-film formation on polycrystalline platinum. *ChemPhyschem* **2012**, *13* (13), 3210−3217.
(59) Tripathi, R.; Yesilbas, G.; Lamprecht, X.; Gandharapu, P.; Bandarenka, A. S.; Dusane, R. O.; Mukhopadhyay, A. Understanding the Electrolyte Chemistry Induced Enhanced Stability of Si Anodes in Li-Ion Batteries based on Physico-Chemical Changes, Impedance, and Stress Evolution during SEI Formation. *J. Electrochem. Soc.* **2023**, *170* (9), 090544.
(60) Yesilbas, G.; Grieve, D.; Rettmann, D.; Gülderen, K.; Bandarenka, A. S.; Yun, J. Impedance Spectroscopy of Lithium Intercalation into Cathode Materials in Coin Cells. *ChemElectrochem* **2024**, *11* (19), No. e202400390.
(61) Cicvarić, K.; Pohlmann, S.; Zhang, B.; Rahmanian, F.; Merker, L.; Gaberšček, M.; Stein, H. S. Fast formation of anode-free Li-metal batteries by pulsed current. *Phys. Chem. Chem. Phys.* **2024**, *26*, 14713.

https://doi.org/10.1021/acs.jpcc.5c07557
J. Phys. Chem. C XXXX, XXX, XXX−XXX